



# Finite Element Model of the Shoulder with Active Rotator Cuff Muscles: Application to Wheelchair Propulsion

Najoua Assila<sup>1,2,3</sup> · Mickaël Begon<sup>1,2</sup> · Sonia Duprey<sup>3</sup>

Received: 6 September 2023 / Accepted: 9 January 2024 / Published online: 20 February 2024  
© The Author(s) under exclusive licence to Biomedical Engineering Society 2024

## Abstract

The rotator cuff is prone to injury, remarkably so for manual wheelchair users. To understand its pathomechanisms, finite element models incorporating three-dimensional activated muscles are needed to predict soft tissue strains during given tasks. This study aimed to develop such a model to understand pathomechanisms associated with wheelchair propulsion. We developed an active muscle model associating a passive fiber-reinforced isotropic matrix with an activation law linking calcium ion concentration to tissue tension. This model was first evaluated against known physiological muscle behavior; then used to activate the rotator cuff during a wheelchair propulsion cycle. Here, experimental kinematics and electromyography data was used to drive a shoulder finite element model. Finally, we evaluated the importance of muscle activation by comparing the results of activated and non-activated rotator cuff muscles during both propulsion and isometric contractions. Qualitatively, the muscle constitutive law reasonably reproduced the classical Hill model force–length curve and the behavior of a transversally loaded muscle. During wheelchair propulsion, the deformation and fiber stretch of the supraspinatus muscle-tendon unit pointed towards the possibility for this tendon to develop tendinosis due to the multiaxial loading imposed by the kinematics of propulsion. Finally, differences in local stretch and positions of the lines of action between activated and non-activated models were only observed at activation levels higher than 30%. Our novel finite element model with active muscles is a promising tool for understanding the pathomechanisms of the rotator cuff for various dynamic tasks, especially those with high muscle activation levels.

**Keywords** Active muscles · Finite element model · Glenohumeral joint · Rotator cuff · Wheelchair

## Introduction

Shoulder function is a “perfect compromise between stability and mobility” [1]. As the glenohumeral joint’s skeletal structure is inherently unstable, muscles, particularly those of the rotator cuff, play a critical role in this compromise [2]. Accordingly, when the upper extremity is subjected to

repeated or heavy loading, the rotator cuff muscles are put under strain, which can lead to injury. For instance, manual wheelchair users, who rely on their upper extremities for mobility and daily activities, have a higher prevalence of rotator cuff injuries than the able-bodied population, particularly for the supraspinatus tendon [3–5]. In a sample of 10 wheelchair users, Morrow et al. [5] observed that this tendon was mostly torn at the anterior portion of the insertion site in the intrasubstance or articular regions. For a larger group (n = 44), Jahanian et al. [6] reported a higher prevalence of tears in the insertion zone at the bursal region in the anterior and middle portions of the tendon. A better understanding of the rotator cuff loading and strain during a given task might help explain the higher prevalence and specificity of the lesion location for manual wheelchair users.

Finite element analysis, being a numerical method adept at resolving intricate problems in continuum mechanics, presents a valuable tool for modeling the mobility of the shoulder complex and assessing the distribution of strain

---

Associate Editor Stefan M. Duma oversaw the review of this article.

---

✉ Najoua Assila  
najoua.assila@umontreal.ca

<sup>1</sup> School of Kinesiology and Exercise Sciences, Faculty of Medicine, University of Montréal, Montréal, QC, Canada

<sup>2</sup> Research Center of the Sainte-Justine University Hospital Center, Montréal, QC, Canada

<sup>3</sup> Univ Lyon, Univ Gustave Eiffel, Univ Claude Bernard Lyon 1, LBMC UMR T\_9406, 69622 Lyon, France

within soft tissues. In their review of shoulder finite element models, Zheng et al. [7] concluded that there is a need for comprehensive dynamic models that account for soft tissue interactions. As boundary conditions greatly influence the simulation results, the model should account for physiological constraints and loading [8]. To this aim, various models have relied on force and kinematics extracted from rigid multi-body models [9–12]. Nevertheless, in these models, the muscle forces were applied either through one-dimensional connector elements [11, 12] or as external vector loads [9, 10]. In the former case, the strain within the muscle volume could not be estimated, while in the latter, the influence of the activated state on the muscle volume was not considered. As muscles contain mostly water, they are nearly-incompressible structures. Therefore, their contraction in the fiber direction results in a wider cross-section [13]. These interactions between the contractile elements and the extracellular matrix may alter muscle force generation [14]. By incorporating these interactions, a finite element model can depict the effect of contacts between structures on the muscle longitudinal force [15, 16], as well as the transmission of forces through connective tissue [17].

To model muscle contraction, some studies associated one-dimensional elements governed by the Hill muscle model with isotropic passive three-dimensional hexahedral elements [16, 18, 19]. However, meshing soft tissue volumes accurately with hexahedral elements is challenging to implement [20], particularly as the element edges should align with fiber trajectories. Another approach is to include the contraction in the continuous constitutive law. In such models, muscles are contracted using a force–length relationship based on the Hill muscle model [21, 22], the Hatze model [23–25], or the calcium chemical equilibrium [26]. The use of the force–length relation can be criticized as the relationship is not continuous in length and time [27]. Both the Hatze and chemical-equilibrium models represent equivalent activation dynamics [28]. Whereas the latter has been mostly implemented to study cardiac muscle, it has the advantage of expressing the physiology behind muscle excitation. As cardiac and skeletal muscles have similar contraction mechanisms [29], this law could be an alternative approach for activating skeletal muscles.

Finite element analysis for modeling shoulder muscles remains underrepresented in current literature. Notably, there is a noticeable lack of finite element shoulder models that incorporate active three-dimensional muscles, whose contraction is based on the physiology of activation dynamics, and not solely using the Hill muscle model. Consequently, this study aimed to develop a model of the shoulder complex with active three-dimensional rotator cuff muscles: the rigid segments, representing the bones, were driven by kinematics extracted through a rigid multibody model; additionally, the modeling of the muscles accounted for their

quasi-incompressibility, anisotropy, and contractility by activating hyper-elastic fibers using experimental electromyography (EMG). We hypothesized that this model would help understand the pathomechanisms of rotator cuff injuries associated with wheelchair propulsion. Thus, our aim was to evaluate if the model can predict regions at risk of injury that align with clinical observations. A secondary hypothesis was that an activated model would lead to differences in the strain distribution within the soft tissue, which might alter the muscles' lines of action. Accordingly, in this article, we will first showcase how the implemented muscle model can predict physiological muscle behavior. Then, we will use the presented muscle model to evaluate rotator cuff strain during manual wheelchair propulsion and explain potential injury pathomechanisms. Finally, we will evaluate the differences in simulation outputs between activated and non-activated muscles to conclude on the importance of muscle activation in finite element muscle modelling.

## Methods

### Muscle Activation Law

As muscles are hyperelastic, nearly-incompressible, and anisotropic entities [20, 30], their structure was modelled as an extracellular isotropic matrix reinforced with fibers [21, 24, 31]. The isotropic energy was a function of the two first principal invariants of the deformation tensor, while the anisotropic energy was a function of the fiber stretch. Nearly-incompressible Ogden [18] and Holzapfel–Gasser–Ogden models [32] were used to model the isotropic and the fiber passive behaviors, respectively. The contractile behavior of the muscle was based on an activation model that describes the relationship between the calcium ion concentration and the tissue tension [33]. This model expresses the chemical equilibrium during muscle contraction at a given sarcomere length as follows [33]:

$$\tau = \frac{[Ca^{2+}]^n}{[Ca^{2+}]^n + [Ca_{50}^{2+}]^n} \tau_{max}, \quad (1)$$

where  $\tau$  is the active fiber Kirchhoff stress,  $\tau_{max}$  is the maximum isometric tension at maximum calcium concentration,  $[Ca^{2+}]$  is the calcium concentration,  $[Ca_{50}^{2+}]$  is the calcium concentration at  $\tau_{max}/2$ , and  $n$  represents the Hill coefficient. As the calcium ion concentration is correlated with the neural excitation intensity [34], and since we only need their relative value to drive this law, we used experimental normalized neural excitation (*i.e.*, normalized EMG) as an input to this model. To account for the length dependency of the sarcomere calcium sensitivity,  $[Ca_{50}^{2+}]$  was expressed as a function of the element length:

$$[Ca_{50}^{2+}] = \frac{[Ca_{max}^{2+}]}{[e^{b(\lambda L - l_0)} - 1]^{1/2}}, \quad (2)$$

where  $b$  is a shape coefficient,  $[Ca_{max}^{2+}]$  is the maximum intracellular calcium concentration,  $\lambda$  the fiber stretch,  $L$  is the optimal element length, and  $l_0$  is a minimal element length.  $l_0$  was adjusted to express that the sarcomere and the muscle cannot generate an active force below a given length [35].

Material laws were implemented using the MAT-295 of the LS-DYNA material library. Passive material constants (i.e., Ogden and Holzapfel–Gasser–Ogden parameters) were calibrated from experimental data [36, 37].  $\tau_{max}$  was calibrated to enable the fully activated muscle to generate a maximal isometric force consistent with values reported in the literature [38].  $[Ca_{max}^{2+}]$  was first bounded between 10 and 16  $\mu\text{mol/L}$  [39]. Then, the parameters  $b$ ,  $n$ , and  $[Ca_{max}^{2+}]$  were adjusted to achieve an electromechanical delay of 20 ms as reported in [40–42], while having  $[Ca_{50}^{2+}]$  values consistent with in-vitro data [43], i.e., between 1 and 2.5  $\mu\text{mol/L}$ . Details of the parameters are provided in the Appendix section (Table 1).

### Investigation of the Activation Law: Simple Muscle Model

To compare the contractile behavior of the implemented model to the classically used Hill muscle model, we evaluated the force–length curve generated with the implemented constitutive law by simulating isometric contractions at various muscle lengths. A simplified fusiform cylindrical muscle was first stretched, and its passive force was evaluated. Then, the muscle was shortened or stretched from 50 to 150% of its initial length at rest ( $L_0$ ). Constrained at this new length, the muscle was fully activated. To reduce simulation time, only a quarter of the cylinder was simulated under planar symmetry constraints (Fig. 1A). The muscle's active force was evaluated by subtracting the passive force from the force measured at the muscle extremities. The muscle isometric force, normalized to its value under no stretch (i.e., the force generated by the fully activated muscle at its initial length  $L_0$ ), was expressed with respect to the muscle stretch (i.e., the muscle length normalized by  $L_0$ ). The predicted curve was compared qualitatively to the Hill model (normalized muscle force versus its normalized length) classically used to express uniaxial muscle behavior. In the chosen implementation of Hill model, active forces were obtained from experimental data of isometric sarcomere force variation with its length [35], while passive forces were expressed as an exponential function [44]. Although the experimental data of the active force–length relationship has been established from frog samples, they agree well with data from the

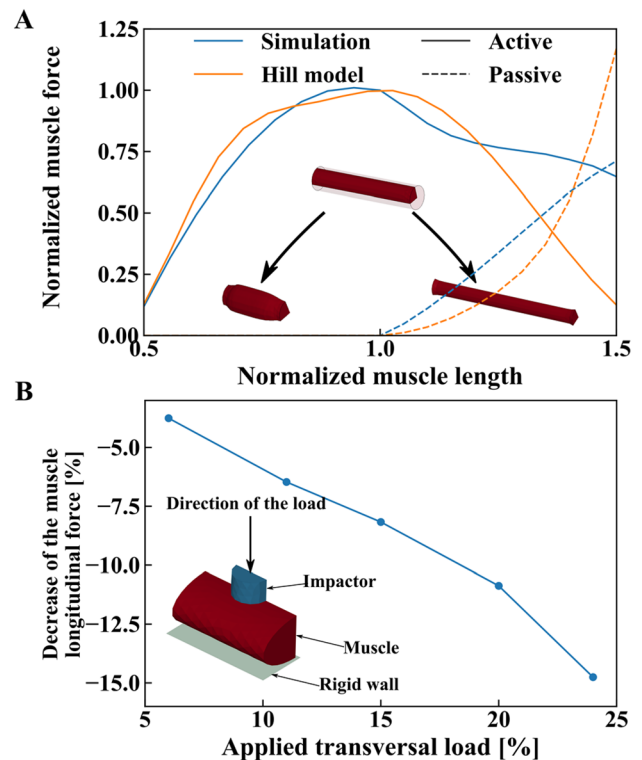


**Fig. 1** A Force–length relationship through finite element simulation (blue) and fitted Hill-model curve from the open access CEINMS toolbox [46]. B Change in muscle longitudinal force when an increasing transversal load is applied. The load and the force changes are expressed as a percentage of the maximal isometric force of the unloaded muscle

human tibialis anterior [45]. We opted to use these active and passive force–length relationships, as they are implemented in the CEINMS toolbox [46], and are often used to model the contraction dynamics in rigid multibody models. The coordinates of these curves were used as a reference to represent the Hill-type muscle model.

One of the motivations behind modeling muscles as three-dimensional structures is to account for the interaction between transversal and longitudinal loads [15]. Accordingly, we evaluated the effect of loading a muscle transversely on the amplitude of its longitudinal force during a maximal isometric contraction, based on the experiment of Siebert et al. [15]. For this second simulation, only half of the muscle was simulated with imposed planar symmetries. The insertion and origin of the muscle were constrained in all degrees of freedom. A load was first applied transversally on the simplified muscle (Fig. 1B). To avoid stress concentration, the load was applied through a rigid cylinder. The magnitude of the applied transversal force ranged from 6 to 24% of the maximal isometric force of the unloaded muscle ( $F_{iso}$ ). This force was measured at the insertion (or origin) of the fully activated transversally-unloaded muscle. With

the load still applied, the muscle was fully activated. The muscle's longitudinal force under various transversal loads  $F_{iso\_loaded}$  was compared with  $F_{iso}$ :

$$\Delta F = \frac{F_{iso\_loaded} - F_{iso}}{F_{iso}} \quad (3)$$

## Wheelchair Propulsion: Shoulder Model

The muscle model presented and evaluated in the previous sections was used to activate the rotator cuff of a shoulder finite element model. As an example of a use case, the model was implemented to predict the rotator cuff strain during manual wheelchair propulsion. This section presents the shoulder finite element model and the experimental data that served as input to the finite element model simulation.

### Finite Element Model Construction

The muscle and bone volumes were constructed from medical imaging of the left shoulder of a 32-year-old participant (mass: 80 kg, height: 1.72 m) with no history of shoulder pathology. The model's geometry details can be found in Hoffmann et al. [47]. Briefly, the model included three bones (clavicle, scapula, and humerus) and four muscle-tendon units (deltoid, supraspinatus, infraspinatus, and subscapularis). As the bones were considered rigid structures, only their surfaces were meshed using triangular shells. Their mass and inertial properties were linked to the rigid nodal structure associated with the bones' nodes. The muscle-tendon unit geometries were discretized using tetrahedral elements for the volume, with an additional surrounding surface mesh representing the epimysium. The epimysium was modelled as a nearly-incompressible isotropic hyperelastic material [36]. Details of the model number of nodes and elements are provided in the Appendix section (Table 2).

Muscles were modelled using the constitutive law presented in the section "Muscle Activation Law". Tendons were modelled as an extracellular isotropic matrix reinforced with collagen fibers [48]. Similar to the muscle model, a nearly-incompressible Ogden [18] and Holzapfel-Gasser-Ogden models [32] were used. To define the muscle-tendon unit fibers trajectories, we simulated a Laplacian flow within the structure volume [30, 48, 49]. The insertion and origin of the muscle indicated the inflow and outflow fluxes, respectively. The rest of the muscle envelope was defined as a slip surface. The simulation results agreed qualitatively with cadaveric observations from Ward et al. [50]. Lastly, the supraspinatus and infraspinatus tendon fusion area was identified. It is a zone where the fibers of both tendons are interwoven with fibers from the coracohumeral ligament [51]. Unable to discern its different components, it was

simplified as an isotropic tendon model. A mesh convergence study, conducted on a fully activated subscapularis muscle, indicated that a decrease by half of the elements' size led to a shift of  $0.48 \pm 0.60$  mm in the position of the lines of action.

### Experimental Data and Boundary Conditions

Muscle electromyography and marker-based motion capture were collected during wheelchair propulsion for the participant presented previously. The research protocol was approved by the Sainte-Justine University Hospital Center Ethics Committee (MP-21-2020-2533). The trunk and right upper limb were tracked using 38 reflective skin markers at 250 Hz. Our motion capture setup consisted of 16 MX-T40S cameras (Vicon, Oxford, UK). Muscle activities were recorded at 2000 Hz using three surface EMG electrodes (Trigno EMG Wireless System, Delsys, USA) for the deltoid muscle (anterior, median, and posterior heads) and using three pairs of indwelling electrodes for the supraspinatus, infraspinatus, and subscapularis.

A static pose was first recorded to anthropometrically scale the musculoskeletal model of Wu et al. [38] in OpenSim [52]. The model included a glenohumeral and an acromioclavicular joint, defined as spherical joints, and a sternoclavicular joint modeled as a 2-DOF universal joint. The participant propelled a manual wheelchair at a comfortable speed over a level surface. From the measured trajectories of the reflective markers, Euler angles of the shoulder joints were estimated using inverse kinematics in OpenSim. The EMG raw signals were first processed using a fourth-order Butterworth bandpass filter (20–500 Hz for the deltoid and 20–600 Hz for rotator cuff muscles, surface and indwelling electrodes, respectively), then full wave rectified. The envelopes were obtained using a 4 Hz fourth-order low-pass filter and then normalized with respect to recorded maximal voluntary contractions (MVC) [53]. During the MVCs, the participant gradually increased his activation before maintaining a plateau for 3 s under verbal encouragement. The MVCs were 1 min apart unless the participant required more rest time. We identified propulsion cycles using the instrumented wheel rotation torque based on a 0.5 N·m threshold. One cycle was randomly chosen to be simulated with the finite element model.

To define physiological boundary conditions on the muscle-tendon units of the shoulder finite element model, the rigid-body model's acromioclavicular and glenohumeral joint kinematics were imposed. Normalized EMG envelopes were used to activate the muscles. As the deltoid had an experimental signal for each head (anterior, median, and posterior) but was only modelled as one component in the finite element model, its activation input was the mean of the three signals. Frictionless contacts were modelled between

the different structures to avoid penetrations. The penalty coefficients between the structures were iteratively adjusted to minimize the sum of the contact energies of the dependent and independent surfaces.

For each of the infraspinatus, supraspinatus, and subscapularis muscles, six lines of actions were defined for post-simulation analysis. These lines passed through the centroids of the muscle's sequential cross-sections [54]. The coordinates of the points of each line were evaluated throughout the propulsion cycle to assess the line of action path and length.

### Effect of Activation: Shoulder Model

To assess the effect of activation on the model outputs, we simulated the propulsion cycle, presented in the previous section with the same shoulder model without activating the muscles. The Euclidian distances between the points of the two models' lines of action were calculated to compare the active (with activated muscles) and passive (without activated muscles) simulations. The distance between the muscle envelopes was also evaluated.

As EMG signals during wheelchair propulsion were expected to be low [55, 56], particularly in comparison with other strenuous wheelchair skills (e.g., ascending an incline or a curb), we also evaluated the effect of rotator cuff activation levels on the simulation outputs. Particularly, we gradually activated each of the infraspinatus, supraspinatus, and subscapularis (25, 50, 75, and 100%) while the bones were kinematically constrained (*i.e.*, static).

## Results

### Investigation of the Activation Law: Simple Muscle Model

The active force–length relationship obtained through simulation reasonably predicted the Hill-model curve, particularly for muscle shortening (Fig. 1A; from 0.5 to 1.0 of normalized length). When the muscle was stretched (1.0–1.5), the decrease in active force was slower in the simulation than in the Hill model. The muscle passive force was initially higher than the experimental data (fiber stretch *i.e.*, normalized muscle length  $\lambda < 1.4$ ), but the passive stiffness increased slower for the simulated data as the stretch increased. When the muscle was subjected to a transverse force, its longitudinal isometric force decreased as the transversal load increased. Particularly, when the applied transversal load was equal to 24% of the isometric force of

the unloaded muscle, the longitudinal force decreased by roughly 15% (Fig. 1B).

### Wheelchair Propulsion: Shoulder Model

The EMG envelope, bone kinematics and predicted muscle deformation at the start and middle of the push and recovery phases are illustrated in Fig. 2. Muscle fibers were more stretched near the tendon-muscle junction (Fig. 3). The amplitude of the stretch within the fiber (0.7–1.6, heatmap scale on Fig. 3) was higher than that of the lines of action stretch (0.9–1.2; plot y-axis on Fig. 3). For the infraspinatus and subscapularis, the stretch increased throughout the fiber directions similarly between cranial and caudal parts. In contrast, the increase for supraspinatus differed between the anterior and posterior sections. This distribution difference was also observed for the active and passive fiber stresses and the Von Mises stresses (Appendix—Fig. 7). Finally, the infraspinatus and subscapularis were mainly stretched or shortened. In contrast, the supraspinatus muscle-tendon unit appeared to be variably twisted during the propulsion cycle (Fig. 4).

### Effect of Activation: Shoulder Model

We found that the activation of the muscles altered minimally the rotator cuff lines of action (differences  $< 0.3$  mm) and the muscle-tendon units' envelopes position throughout the propulsion cycle (Fig. 5). Similarly, minimal differences were observed in the stretch ( $< 3e-3$ ), passive stress along the fiber ( $< 1$  kPa), and Von Mises stress within the isotropic matrix ( $< 15$  kPa, Appendix—Fig. 8). Similar observations can be made at lower activation levels (*i.e.*, 25%) for the isometric contractions' simulation, where indeed meaningful differences were not observed at 25% contraction but increased significantly for higher activation levels (Fig. 6). Particularly, the differences were observed for the three muscles' lines of action (up to 5 mm) and between their envelopes (up to 11 mm). Additionally, the variability of the distance between the six lines of action increased with the activation level, which indicates differences in the muscle cross-section shape. Notably, the differences in the shape of muscle-tendon unit volumes were the largest at the tendon-muscle junction. Finally, as the activation increased, the tendons of the activated model were more stretched, which led to a concentration of the passive fiber stress in these structures and an increase in the Von Mises stresses.

**Fig. 2** **A** EMG signal used to activate the muscles. The deltoid EMG represents the average of the signal measured from the anterior, median, and posterior heads. **B** Finite element simulation output for the activated shoulder model in four key moments of a wheelchair propulsion cycle, with **C** a schematic of the wheelchair user

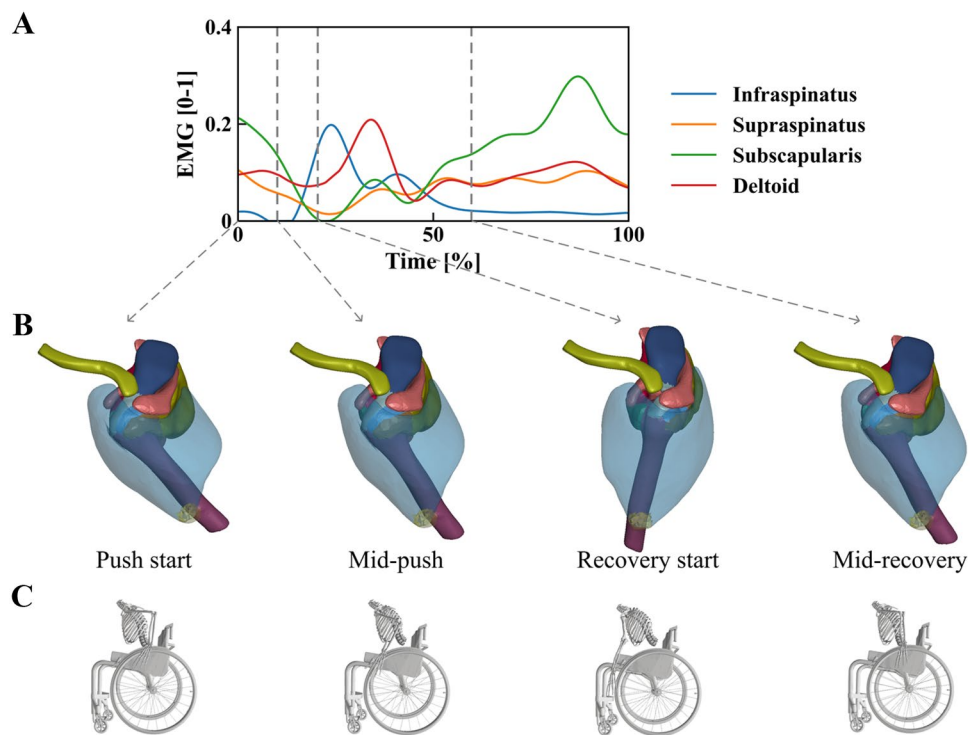
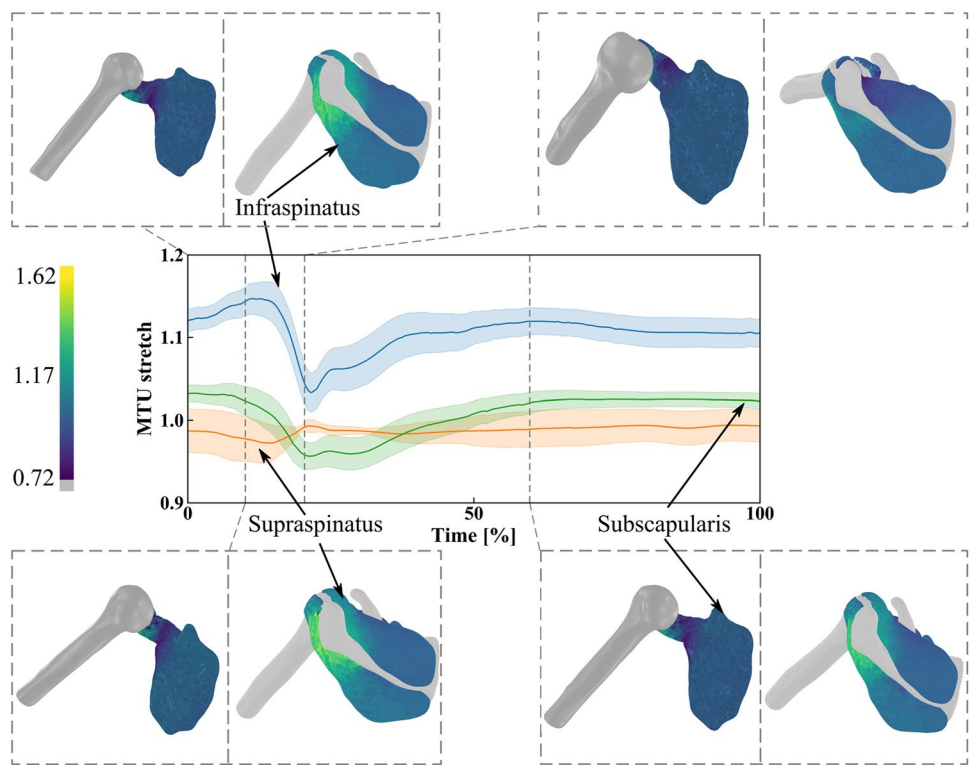


**Fig. 3** Muscle-tendon unit (MTU) stretches throughout the propulsion cycle for the infraspinatus, supraspinatus and subscapularis. The solid line and the transparent corridor represent the mean stretch between the six lines of action and their standard deviation, respectively. The vertical dashed lines indicate, in order, the time of mid-push, recovery start, and mid-recovery. The fiber stretch distributions for the infraspinatus, supraspinatus (right), and subscapularis (left) muscles are represented using a color map. The subscapularis is viewed from the posterior side, *i.e.*, the viewed surface is the one in contact with the scapula



**Discussion**

We developed a finite-element model of the glenohumeral joint featuring three-dimensional active rotator cuff muscles.

Muscle contraction was simulated using experimental EMG signals, while joint angles were predicted from marker trajectories. Our research revealed significant findings: (i) the applied muscle activation law demonstrated its applicability

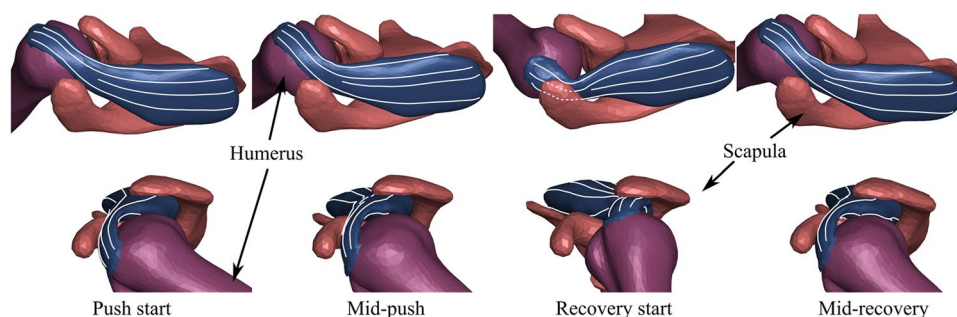


**Fig. 4** Supraspinatus muscle-tendon unit (blue) at different steps of the propulsion cycle from top and left side views (rows). The reader can refer to Fig. 2 for a complete representation of the bones' con-

figuration. The white lines within the muscle-tendon unit volume represent some of the fibers' directions. The supraspinatus seems to be twisted in different directions throughout the cycle

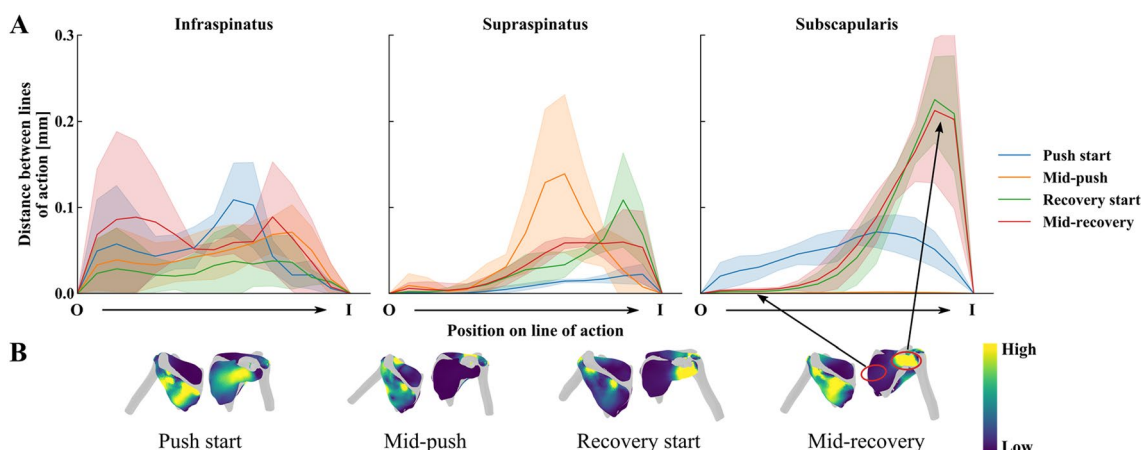


**Fig. 5** **A** Distance between the rotator cuff lines of action predicted by the active and passive models (mean of six lines of action  $\pm$  standard deviation: solid line  $\pm$  transparent band). Each line shows the difference at a given state (color) from origin (O) to insertion (I). **B** Schematic of the differences between the muscle envelopes between the models. At each presented time event, the schematics show the posterior view with the infraspinatus and supraspinatus (left) and

the anterior view with the subscapularis muscle (right) view of the model. These views explain the shape of the curves in **A**. For instance, in **A**, the subscapularis difference is highest near its insertion at the start and mid-recovery, which is consistent with the yellow-colored area on its schematic in **B**, as indicated in the third column

to skeletal muscle by reasonably predicting the force-length muscle relationship; (ii) analysis of strain distribution and muscle deformation aligned with clinically observed shoulder lesions in manual wheelchair users, supporting our initial hypothesis; however, (iii) our secondary hypothesis was not substantiated, highlighting the task-dependent nature of muscle activation's importance in finite-element simulation. For instance, during isometric contractions of the rotator cuff muscles, activation seems to play a critical role in the model's output, when exceeding 30%.

### The Muscle Activation Law

The model predicted reasonably well the behavior of the muscle during isometric activation at different fiber lengths. Nevertheless, the predictions on the muscle shortening phase

were closer to the Hill model, than those on the stretching phase. This difference in fit quality can be explained by the interactions between the passive and active components of the muscle constitutive law. Indeed, the scaling of the activation from element tension to muscle force depends on the equilibrium between passive fiber and extracellular matrix constraints and the activation tension. Unlike muscle shortening, when the muscle is stretched, the potentials related to the isotropic extracellular matrix and its incompressibility increase their contribution to the muscle force [57]. Thus, the passive components assist the active ones in resisting lengthening. The difference in the force prediction accuracy between shortening and stretching can point to a need to optimize the parameters of the passive constitutive law. Identifying numerical values for parameters of the passive law is not an easy task. Indeed, the passive mechanical

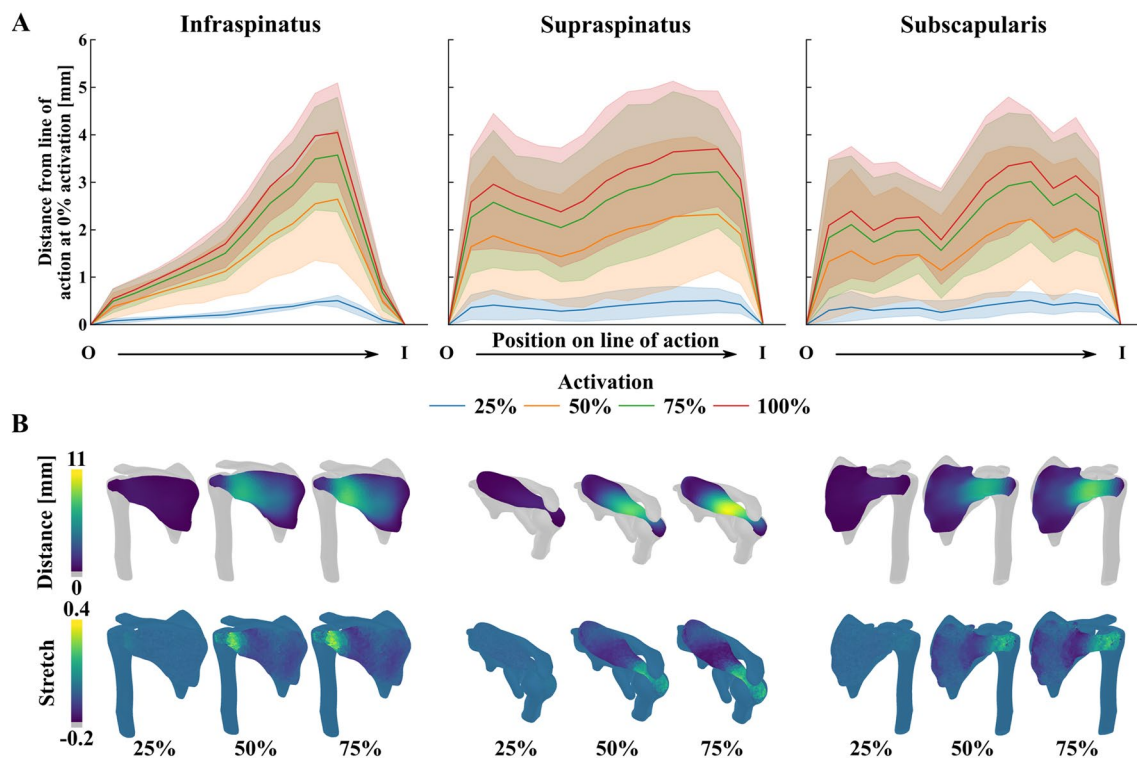


**Fig. 6** **A** Changes in the position of the rotator cuff lines of action as the muscles are isometrically contracted at 25, 50, 75, and 100%. The line of action is discretized as points from the muscle's origin (O) to its insertion (I, x-axis from left to right). Each drawn line (color for the level of activation) represents the shift in the position of the lines of action as the muscle is contracted (mean of six lines

of action  $\pm$  standard deviation: solid line  $\pm$  transparent band). Accordingly, as the muscles' origins are fixed, they remain at the same position (*i.e.*, at 0). **B** Schematic of the distance between the muscle envelopes (top) as well as the differences in fiber stretch (bottom). As the state of full activation (100%) is qualitatively similar to that at 75% activation, its schematic was not represented

properties depend on the muscle [58], its size scale (fiber, bundle, muscle) [59], age [60], and neuromuscular pathologies [61]. Hence, in the presence of in-vivo data, adjusting the parameters to account for the model's size and origin would be recommended. Additionally, to account for the interactions between the active and passive components of a muscle, the passive parameters should go through an additional optimization step, where the normalized passive muscle force is fitted to the expected passive behavior of a muscle.

The maximum isometric muscle force occurred at a shorter normalized length ( $\lambda \approx 0.9$ ; Fig. 1A). Indeed, optimal length was defined at the element level in the constitutive law. For the muscle's optimal length to coincide with the muscle length, all elements should have the same activation level and fiber's stretch. However, as the contractions were isometric, the extracellular matrix would distribute the stress gradually from the muscle-constrained edges towards its center. Elements reached equilibrium at slightly different stretches. Indeed, Moo et al. [62] observed that the non-uniformities of sarcomere lengths during in-vivo muscle activation led to a longitudinal measured force ranging from 65 to 116% of the theoretical isometric force. Additionally,

through simulation, Wakeling et al. [57] concluded that a muscle could not contract with all its fibers at their optimal length, as its most energetically favorable state occurs with a slight expansion in the transverse direction.

The physiological behavior of the implemented muscle model was further validated through the observed decrease of its longitudinal force when the muscle was subjected to a transversal loading (Fig. 1B). This decrease was coherent with the ex-vivo behavior reported for isolated short muscles at low pennation angles [15, 63]. Unlike other models [13, 64], the chosen activation law did not explicitly link the longitudinal amplitude to the transverse loading. Nevertheless, the isotropic component of the deformation energy enables the model to decrease the longitudinal muscle force while resisting the muscle compression imposed by the external load [65]. Assuming a weight is used to apply this external load, this resistance can be seen as a lifting force that would move the impactor (Fig. 1B). Unlike Siebert et al. [15], we did not observe a significant change in the impactor lifting height with the amplitude of the transverse load. However, this might be explained by our implementation of a simplified muscle volume, particularly as the relative deformation



in the transversal section can vary between muscles and with muscle stress asymmetries [13, 57, 65].

### Propulsion and Rotator Cuff Injury

The length variation of the rotator cuff muscles throughout the propulsion cycle was minimal (0.9–1.2 stretch). This finding is consistent with the rotator cuff muscles' architecture and function, as they are optimized to work around their optimal length throughout the glenohumeral range of motion to ensure its stability [50]. On the other hand, the local stretch was larger, notably near the myotendinous junction, which is consistent with in-vivo observations that sarcomeres stretch more near the distal myotendinous junction [66]. These high stretches at the tendon might lead to microscopic tears due to the collagen fibrils sliding [67–69]. The stretch of the supraspinatus differed between its anterior and posterior portions during most of the cycle, as the tendon was deformed to accommodate contact with the scapula. These differences in stretch and, subsequently, in stress could partly explain the higher prevalence of supraspinatus lesions. Indeed, its posterior and anterior portions vary in elasticity and ultimate failure load [70, 71]. Additionally, as both portions can move independently [72], the resulting shear stress in the extracellular matrix could lead to delamination, as observed between the articular and bursal sides of the tendon during abduction [73]. Such a mechanism could partially explain the presence of lesions in the middle portions of the tendon [6]. Moreover, the repetitive compression and bending of the anterior part (Fig. 4) are known to be linked to compromised vascularization [74, 75], which was correlated with rotator cuff degeneration [76]. This mechanism could explain the higher prevalence of anterior lesions in manual wheelchair users [5, 6].

Finally, the repetitive and compressive load on the tendon may lead to water depletion [77], which would reduce the tendon thickness. This thickness reduction was reported for manual wheelchair users after a fatiguing protocol [78]. With repetitive complex loading of the supraspinatus tendon, the water loss might provoke an increase in proteoglycans in the tendon extracellular matrix, a characteristic process in tendinopathy [79, 80]. Indeed, one of the supraspinatus tendon characteristics is the presence of large proteoglycan accumulate that might help lubricate the tendon to facilitate its collagen fibers sliding [81]. With increased bending and twisting, the tendon changes its structure, initially optimized for tensile stress, by increasing the accumulation of large proteoglycan aggrecan [82]. This change leads to a decrease in type I collagen synthesis, which is the main constituent of the tendon fibrils [83]. As the supraspinatus tendon is not thicker for wheelchair users with rotator cuff tendinopathy [84], nor after intense propulsion tasks [85–87], propulsion might not generate tendon inflammation. Thus, the change

in the tendon structure is most probably not accompanied by inflammation. Consequently, supraspinatus tendinopathy might be more of a tendinosis due to the repeated tendon stretch and twisting observed in the simulation results [88]. Tendinosis treatment aims to break the cycle of injury and can take from 6 weeks to 6 months to allow the synthesis of new healthy collagen [89]. This required duration might explain the high prevalence of injury for manual wheelchair users who are constantly propelling themselves, with an average of 90 bouts per day [90], never allowing the tendon to heal properly. As tendon cellular damage seems inevitable for this population, continuous eccentric strengthening exercises, massages, stretching, and an adjusted diet might help decrease pain and increase tendon strength [88]. The simulation results of the presented hybrid shoulder model (*i.e.*, the combination of rigid bodies and finite element models) enabled us to highlight potential pathomechanisms of the supraspinatus tendon that are consistent with the clinical literature [5, 6]. Additionally, we hypothesized that the supraspinatus is prone to tendinosis, which could help clinicians adjust the rehabilitation protocol of manual wheelchair users. Nevertheless, for the simulated task (*i.e.*, wheelchair propulsion), the muscle activation did not seem to alter the model outputs, raising the question on the importance of muscle activation for models of the rotator cuff muscle.

### Is Activation Necessary?

Similar to previous studies [55, 56], the experimental EMG signal throughout the propulsion cycle was below 30%. At this activation level, and since the skeletal kinematics partially imposed the fiber' stretches, the active stress was inferior to the passive stresses (Appendix—Fig. 7). Thus, its contribution to the dynamics equations within the muscle was relatively minimal, which would explain the minimal differences between the active and passive model during wheelchair propulsion. This was also the case at low activation levels (*i.e.*, 25%) for the isometric maximal contraction simulation. Similarly to these findings, the lack of meaningful differences between active and passive models for low activation tasks can also be inferred from the literature, where moment arms of the rotator cuff muscles obtained from passive [47] and active [30] shoulder models were similar during unloaded shoulder elevations. Accordingly, a passive model could be sufficient for assessing rotator cuff muscle trajectories and moment arms during low activation tasks. However, for higher activation tasks, the muscle constitutive law should account for muscle activation, as the latter considerably modifies the muscle shape and its local stretch distribution (Fig. 6). Thus, implementing the activated model to study wheelchair propulsion during more demanding tasks such as curb or incline ascents [91, 92] might enhance

our understanding of rotator cuff pathomechanisms related to daily mobility. Other factors that might influence the importance of integrating activation are the task dynamic parameters. Indeed, different studies highlighted the shift in muscle function, based on mechanical work [93, 94], in response to changes in velocity or load. Thus, depending on the muscle-length change during the task (*e.g.*, isometric, slow eccentric contractions), the stiffness of the passive structure would change, which might affect the level at which the influence of the activation on the strain distribution becomes tangible. Finally, since most muscle trajectories in rigid body models are extracted from cadaveric data, it would be interesting to evaluate the effect of activation on their predicted muscle and joint reaction forces, as moment arms are expected to change significantly with the increased muscle activation. Through the evaluation of simulation results as a function of muscle activation levels, we were able to draw conclusions on the task-dependent importance of the inclusion of muscle contractility in muscle finite element constitutive laws. Nevertheless, it remains to confirm if these conclusions are valid for longer muscles (*e.g.*, biceps) as the latter sustain larger deformations with activation.

This study had some limitations. First, despite our model's increased complexity, it included several simplifications. The soft tissues' viscoelasticity was neglected; the passive structures (ligaments, labrum, and joint capsule) were not modelled, nor were the different parts of the muscles and tendons, identified through cadaveric studies [50], differentiated. Including the passive structures might add contact constraints to the rotator cuff muscles, such as the ones expected when in the case of an impingement. Nevertheless, the risk for the latter to occur during propulsion remains relatively low [95]. The glenohumeral joint translation was also constrained; and the bone kinematics were not the result of the muscle actions. Nevertheless, the presented model can be modulated to increase its complexity, depending on the purpose of its implementation. For instance, other muscles of the shoulder complex could be modelled as Hill-type lines of action. Within this new augmented model, the joint reaction forces could either be imposed as constraints, or compared as simulation outputs to their values as predicted by the rigid-body model. The latter approach could

then be considered an additional validation of the hybrid finite element model. Secondly, a limit relatively common for finite element simulation was the long calculation time, where a 2.48 s simulation required about 52 hours, irrespective of the muscle activation status, using a laptop with 4 Intel® i7-8750H 2.20 GHz processors. Finally, while the qualitative validation of the constitutive law was promising, the shoulder model results were not directly validated. For future studies, simpler tasks, such as sub-maximal isometric activation at various shoulder positions, could be simulated to compare simulation strains and displacements to ones obtained from MRI. However, we are confident that the model presented holds significant promise for providing valuable insights into rotator cuff function and the associated risk of injury. This model serves as a valuable tool for the research community to explore inquiries regarding the impact of alterations in scapulothoracic rhythm on the strain imposed on the rotator cuff. For instance, it can be utilized to assess whether depressing the shoulder genuinely reduces the risk of shoulder pain or, conversely, increases strain on the soft tissues.

This study aimed to implement a finite element model of the shoulder with three-dimensional activated muscles. The activation law reasonably predicted the skeletal muscle's force-length relationship and the interaction between a muscle's longitudinal and transverse forces. By analyzing the supraspinatus tendon deformation during a manual wheelchair propulsion cycle, we could offer possible explanations for the localization and prevalence of tendon tears for wheelchair users, which indicates that this model could be implemented in the future to improve our understanding of rotator cuff pathomechanisms at various tasks. Finally, by evaluating the effect of muscle activation levels on the output of the simulations, we concluded on the task-dependent importance of including activation in the muscle constitutive law.

## Appendix

See Tables 1, 2, Figs. 7 and 8.

**Table 1** Constitutive model parameter

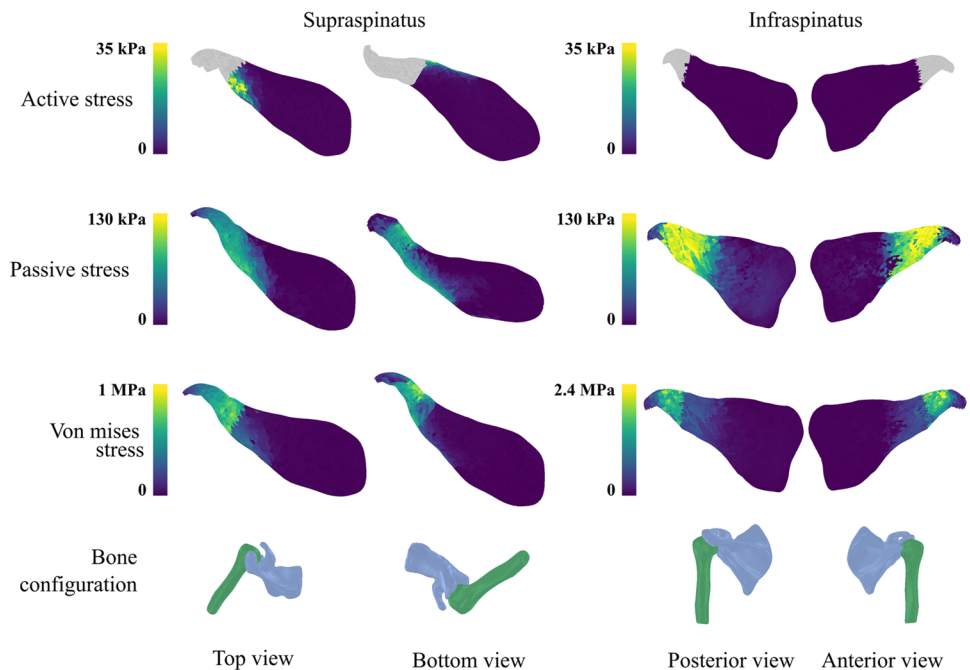
		Material constants
Aponeurosis	Cubic isotropic hyperelastic	$C_{10} = 30\text{N/cm}^2$ $C_{20} = 80\text{N/cm}^2$ $C_{30} = 800\text{N/cm}^2$
Tendon	Extracellular isotropic matrix reinforced with fibers	$\mu_1 = 0.1522; \alpha_1 = 2$ $\mu_2 = 0.3846; \alpha_2 = -2$ $\mu_3 = 0.376; \alpha_3 = 4$ $\mu_4 = -2e - 3; \alpha_4 = -4$ $k_1 = 0.17763$ $k_2 = -0.16091$
Muscles	Isotropic matrix: Ogden	$\mu_1 = 0.01522; \alpha_1 = 2$ $\mu_2 = 0.03846; \alpha_2 = -2$ $\mu_3 = 0.0376; \alpha_3 = 4$ $\mu_4 = -2e - 5; \alpha_4 = -4$
	Fibers—passive: Holzapfel–Gasser–Ogden	$k_1 = 0.17763$ $k_2 = -0.16091$
	Fibers—active	$[Ca_{max}^{2+}] = 15 \mu\text{mol/L}$ $n = 8$ $b = 1.6$ $L = 3$ $l_0 = 1.59$

The parameters are based on previous studies [36, 37, 39–43, 48]

**Table 2** Summary of the number of nodes, shell and solid elements of the shoulder finite element mode

	Bones			Muscle and tendons			
	Clavicle	Scapula	Humerus	Deltoid	Infraspinatus	Supraspinatus	Subscapularis
Nodes	3000	3000	3000	2591	2686	2974	2538
Shell elements	1502	1502	1502	3566	3306	3734	3460
Solid elements	–	–	–	9427	10,336	11,499	9431

**Fig. 7** Different stresses distribution for the supraspinatus (top view: left and bottom view: right) and the infraspinatus (posterior view: left and anterior view: right) muscle-tendon units at the push start. The active and passive stresses are associated with the fibers active and passive tensors along the direction of the fibers, while the Von Mises stress represents the stress in the isotropic muscle matrix. The bottom row represents the humerus (green) and the scapula (blue) associated with the view from which the muscles are represented. For the top two rows, both muscles share the same stress scale



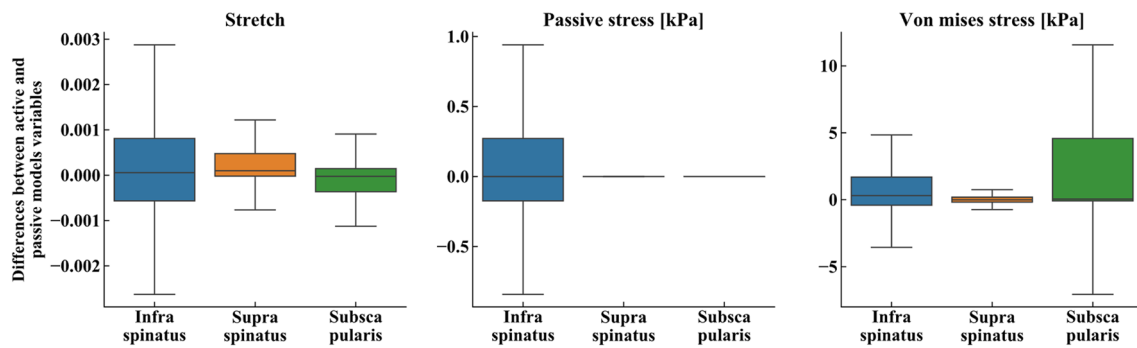


**Fig. 8** Differences between the active and passive models' stretch, passive fiber stress, and the von Mises stress in the isotropic matrix (from left to right) during the wheelchair propulsion cycle. The hori-

zontal line indicates the median value; the boxes represent the interquartile range of the data ( $IQR = [Q1, Q3]$ ); and the whiskers display the data within  $[Q1 - 1.5 \times IQR, Q3 + 1.5 \times IQR]$

**Acknowledgments** This research was undertaken thanks, in part to funding from the Canada First Research Excellence Fund through the TransMedTech Institute, and to the funding of Campus France through the Eiffel scholarship for excellence. This study was carried out within the framework of the Associated International Laboratory EVASYM.

## Declarations

**Competing Interests** The authors have no competing interests to declare that are relevant to the content of this article.

## References

1. Veeger, H. E. J., and F. C. T. van der Helm. Shoulder function: the perfect compromise between mobility and stability. *J. Biomech.* 40(10):2119–2129, 2007. <https://doi.org/10.1016/j.jbiomech.2006.10.038>.
2. Culham, E., and M. Peat. Functional anatomy of the shoulder complex. *J. Orthop. Sports Phys. Ther.* 18(1):342–350, 1993. <https://doi.org/10.2519/jospt.1993.18.1.342>.
3. Akbar, M., et al. Prevalence of rotator cuff tear in paraplegic patients compared with controls. *J. Bone Jt. Surg.* 92(1):23–30, 2010. <https://doi.org/10.2106/JBJS.H.01373>.
4. Arnet, U., et al. MRI evaluation of shoulder pathologies in wheelchair users with spinal cord injury and the relation to shoulder pain. *J. Spinal Cord Med.* 2021. <https://doi.org/10.1080/10790268.2021.1881238>.
5. Morrow, M. M. B., M. G. Van Straaten, N. S. Murthy, J. P. Braman, E. Zanella, and K. D. Zhao. Detailed shoulder MRI findings in manual wheelchair users with shoulder pain. *BioMed Res. Int.* 2014:e769649, 2014. <https://doi.org/10.1155/2014/769649>.
6. Jahanian, O., et al. Shoulder magnetic resonance imaging findings in manual wheelchair users with spinal cord injury. *J. Spinal Cord Med.* 2020. <https://doi.org/10.1080/10790268.2020.1834774>.
7. Zheng, M., Z. Zou, P. Jorge D. Silva Bartolo, C. Peach, and L. Ren. Finite element models of the human shoulder complex: a review of their clinical implications and modelling techniques: finite element models of human shoulder complex. *Int. J. Numer. Methods Biomed. Eng.* 33(2):e02777, 2017. <https://doi.org/10.1002/cnm.2777>.
8. Speirs, A. D., M. O. Heller, G. N. Duda, and W. R. Taylor. Physiologically based boundary conditions in finite element modelling. *J. Biomech.* 40(10):2318–2323, 2007. <https://doi.org/10.1016/j.jbiomech.2006.10.038>.
9. Wei, Y., Z. Zou, G. Wei, L. Ren, and Z. Qian. Subject-specific finite element modelling of the human hand complex: muscle-driven simulations and experimental validation. *Ann. Biomed. Eng.* 2019. <https://doi.org/10.1007/s10439-019-02439-2>.
10. Zheng, M., Z. Qian, Z. Zou, C. Peach, M. Akrami, and L. Ren. Subject-specific finite element modelling of the human shoulder complex part 1: model construction and quasi-static abduction simulation. *J. Bionic Eng.* 17(6):1224–1238, 2020. <https://doi.org/10.1007/s42235-020-0098-0>.
11. Navacchia, A., D. R. Hume, P. J. Rullkoetter, and K. B. Shelburne. A computationally efficient strategy to estimate muscle forces in a finite element musculoskeletal model of the lower limb. *J. Biomech.* 84:94–102, 2019. <https://doi.org/10.1016/j.jbiomech.2018.12.020>.
12. Sadeqi, S., A. P. Baumann, V. K. Goel, V. Lilling, and S. J. L. Sullivan. A validated open-source shoulder finite element model and investigation of the effect of analysis precision. *Ann. Biomed. Eng.* 51(1):24–33, 2023. <https://doi.org/10.1007/s10439-022-03018-8>.
13. Randhawa, A., and J. M. Wakeling. Multidimensional models for predicting muscle structure and fascicle pennation. *J. Theor. Biol.* 382:57–63, 2015. <https://doi.org/10.1016/j.jtbi.2015.06.001>.
14. Roberts, T. J., et al. The multi-scale, three-dimensional nature of skeletal muscle contraction. *Physiology.* 34(6):402–408, 2019. <https://doi.org/10.1152/physiol.00023.2019>.
15. Siebert, T., O. Till, N. Stutzig, M. Günther, and R. Blickhan. Muscle force depends on the amount of transversal muscle loading. *J. Biomech.* 47(8):1822–1828, 2014. <https://doi.org/10.1016/j.jbiomech.2014.03.029>.
16. Stelletta, J., R. Dumas, and Y. Lafon. Chapter 23—modeling of the thigh: a 3D deformable approach considering muscle interactions. In: *Biomechanics of Living Organs*, edited by Y. Payan, and J. Ohayon, vol. 1, in *Translational Epigenetics*, vol. 1, Oxford: Academic Press, 2017, pp. 497–521. <https://doi.org/10.1016/B978-0-12-804009-6.00023-7>.
17. Purslow, P. P. The structure and role of intramuscular connective tissue in muscle function. *Front. Physiol.* 2020. <https://doi.org/10.3389/fphys.2020.00495>.
18. Mo, F., F. Li, M. Behr, Z. Xiao, G. Zhang, and X. Du. A lower limb-pelvis finite element model with 3D active muscles. *Ann. Biomed. Eng.* 46(1):86–96, 2018. <https://doi.org/10.1007/s10439-017-1942-1>.

19. Mo, F., J. Li, M. Dan, T. Liu, and M. Behr. Implementation of controlling strategy in a biomechanical lower limb model with active muscles for coupling multibody dynamics and finite element analysis. *J. Biomech.* 91:51–60, 2019. <https://doi.org/10.1016/j.jbiomech.2019.05.001>.
20. Blemker, S. S. Chapter 17—three-dimensional modeling of active muscle tissue: the why, the how, and the future. In: *Biomechanics of Living Organs*, edited by Y. Payan, and J. Ohayon, vol. 1, in *Translational Epigenetics*, vol. 1. Oxford: Academic Press, 2017, pp. 361–375. <https://doi.org/10.1016/B978-0-12-804009-6.00017-1>.
21. Blemker, S. S., P. M. Pinsky, and S. L. Delp. A 3D model of muscle reveals the causes of nonuniform strains in the biceps brachii. *J. Biomech.* 38(4):657–665, 2005. <https://doi.org/10.1016/j.jbiomech.2004.04.009>.
22. Zeng, W., et al. Modeling of active skeletal muscles: a 3D continuum approach incorporating multiple muscle interactions. *Front. Bioeng. Biotechnol.* 2023. <https://doi.org/10.3389/fbioe.2023.1153692>.
23. Hatze, H. A general myocybernetic control model of skeletal muscle. *Biol. Cybern.* 28(3):143–157, 1978. <https://doi.org/10.1007/BF00337136>.
24. Röhrle, O., M. Sprenger, and S. Schmitt. A two-muscle, continuum-mechanical forward simulation of the upper limb. *Biomech. Model. Mechanobiol.* 16(3):743–762, 2017. <https://doi.org/10.1007/s10237-016-0850-x>.
25. Ramasamy, E., et al. An efficient modelling-simulation-analysis workflow to investigate stump-socket interaction using patient-specific, three-dimensional, continuum-mechanical, finite element residual limb models. *Front. Bioeng. Biotechnol.* 2018. <https://doi.org/10.3389/fbioe.2018.00126>.
26. Zhang, Y., et al. A novel MRI-based finite element modeling method for calculation of myocardial ischemia effect in patients with functional mitral regurgitation. *Front. Physiol.* 11:158, 2020. <https://doi.org/10.3389/fphys.2020.00158>.
27. Rassier, D. E., B. R. MacIntosh, and W. Herzog. Length dependence of active force production in skeletal muscle. *J. Appl. Physiol.* 86(5):1445–1457, 1999. <https://doi.org/10.1152/jappl.1999.86.5.1445>.
28. Rockenfeller, R., and M. Günther. Inter-filament spacing mediates calcium binding to troponin: a simple geometric-mechanistic model explains the shift of force-length maxima with muscle activation. *J. Theor. Biol.* 454:240–252, 2018. <https://doi.org/10.1016/j.jtbi.2018.06.009>.
29. Adams, R. J., and A. Schwartz. Comparative mechanisms for contraction of cardiac and skeletal muscle. *Chest.* 78(1, Supplement):123–139, 1980. [https://doi.org/10.1378/chest.78.1\\_Supplement.123](https://doi.org/10.1378/chest.78.1_Supplement.123).
30. Webb, J. D., S. S. Blemker, and S. L. Delp. 3D finite element models of shoulder muscles for computing lines of actions and moment arms. *Comput. Methods Biomech. Biomed. Eng.* 17(8):829–837, 2014. <https://doi.org/10.1080/10255842.2012.719605>.
31. Lemos, R. R., J. Rokne, G. V. G. Baranoski, Y. Kawakami, and T. Kurihara. Modeling and simulating the deformation of human skeletal muscle based on anatomy and physiology. *Comput. Animat. Virtual Worlds.* 16(3–4):319–330, 2005. <https://doi.org/10.1002/cav.83>.
32. Holzapfel, G. A., and R. W. Ogden. Constitutive modelling of passive myocardium: a structurally based framework for material characterization. *Philos. Trans. R. Soc. A: Math. Phys. Eng. Sci.* 367(1902):3445–3475, 2009. <https://doi.org/10.1098/rsta.2009.0091>.
33. Guccione, J. M., and A. D. McCulloch. Mechanics of active contraction in cardiac muscle: part I—constitutive relations for fiber stress that describe deactivation. *J. Biomech. Eng.* 115(1):72–81, 1993. <https://doi.org/10.1115/1.2895473>.
34. van Zandwijk, J. P., M. F. Bobbert, G. C. Baan, and P. A. Huijting. From twitch to tetanus: performance of excitation dynamics optimized for a twitch in predicting tetanic muscle forces. *Biol. Cybern.* 75(5):409–417, 1996. <https://doi.org/10.1007/s004220050306>.
35. Gordon, A. M., A. F. Huxley, and F. J. Julian. The variation in isometric tension with sarcomere length in vertebrate muscle fibres. *J. Physiol.* 184(1):170–192, 1966. <https://doi.org/10.1113/jphysiol.1966.sp007909>.
36. Chi, S.-W., et al. Finite element modeling reveals complex strain mechanics in the aponeuroses of contracting skeletal muscle. *J. Biomech.* 43(7):1243–1250, 2010. <https://doi.org/10.1016/j.jbiomech.2010.01.005>.
37. Winters, T. M., M. Takahashi, R. L. Lieber, and S. R. Ward. Whole muscle length-tension relationships are accurately modeled as scaled sarcomeres in rabbit hindlimb muscles. *J. Biomech.* 44(1):109–115, 2011. <https://doi.org/10.1016/j.jbiomech.2010.08.033>.
38. Wu, W., P. V. S. Lee, A. L. Bryant, M. Galea, and D. C. Ackland. Subject-specific musculoskeletal modeling in the evaluation of shoulder muscle and joint function. *J. Biomech.* 49(15):3626–3634, 2016. <https://doi.org/10.1016/j.jbiomech.2016.09.025>.
39. Rockenfeller, R., and M. Günther. Hill equation and Hatze’s muscle activation dynamics complement each other: enhanced pharmacological and physiological interpretability of modelled activity-pCa curves. *J. Theor. Biol.* 431:11–24, 2017. <https://doi.org/10.1016/j.jtbi.2017.07.023>.
40. Cavanagh, P. R., and P. V. Komi. Electromechanical delay in human skeletal muscle under concentric and eccentric contractions. *Eur. J. Appl. Physiol.* 42(3):159–163, 1979. <https://doi.org/10.1007/BF00431022>.
41. Go, S. A., W. J. Litchy, L. Q. Evertz, and K. R. Kaufman. Evaluating skeletal muscle electromechanical delay with intramuscular pressure. *J. Biomech.* 76:181–188, 2018. <https://doi.org/10.1016/j.jbiomech.2018.05.029>.
42. Thelen, D. G. Adjustment of muscle mechanics model parameters to simulate dynamic contractions in older adults. *J. Biomech. Eng.* 125(1):70–77, 2003. <https://doi.org/10.1115/1.1531112>.
43. Konhilas, J. P., T. C. Irving, and P. P. de Tombe. Length-dependent activation in three striated muscle types of the rat. *J. Physiol.* 544(Pt 1):225–236, 2002. <https://doi.org/10.1113/jphysiol.2002.024505>.
44. Lloyd, D. G., and T. F. Besier. An EMG-driven musculoskeletal model to estimate muscle forces and knee joint moments in vivo. *J. Biomech.* 36(6):765–776, 2003. [https://doi.org/10.1016/S0021-9290\(03\)00010-1](https://doi.org/10.1016/S0021-9290(03)00010-1).
45. Raiteri, B. J., L. Lauret, and D. Hahn. The force-length relation of the young adult human tibialis anterior. *PeerJ.* 11:e15693, 2023. <https://doi.org/10.7717/peerj.15693>.
46. Pizzolato, C., et al. CEINMS: a toolbox to investigate the influence of different neural control solutions on the prediction of muscle excitation and joint moments during dynamic motor tasks. *J. Biomech.* 48(14):3929–3936, 2015. <https://doi.org/10.1016/j.jbiomech.2015.09.021>.
47. Hoffmann, M., M. Begon, Y. Lafon, and S. Duprey. Influence of glenohumeral joint muscle insertion on moment arms using a finite element model. *Comput. Methods Biomech. Biomed. Eng.* 2020. <https://doi.org/10.1080/10255842.2020.1789606>.
48. Quental, C., J. Folgado, J. Monteiro, and M. Sarmiento. Full-thickness tears of the supraspinatus tendon: a three-dimensional finite element analysis. *J. Biomech.* 49(16):3962–3970, 2016. <https://doi.org/10.1016/j.jbiomech.2016.11.049>.
49. Choi, H. F., and S. S. Blemker. Skeletal muscle fascicle arrangements can be reconstructed using a Laplacian vector field

- simulation. *PLoS ONE*.8(10):e77576, 2013. <https://doi.org/10.1371/journal.pone.0077576>.
50. Ward, S., et al. Rotator cuff muscle architecture: implications for glenohumeral stability. *Clin. Orthop. Relat. Res.* 448:157–163, 2006. <https://doi.org/10.1097/01.blo.0000194680.94882.d3>.
  51. Clark, J. M., and D. T. Harryman 2nd. Tendons, ligaments, and capsule of the rotator cuff. Gross and microscopic anatomy. *J. Bone Jt. Surg.* 74(5):713–725, 1992.
  52. Delp, S. L., et al. OpenSim: open-source software to create and analyze dynamic simulations of movement. *IEEE Trans. Biomed. Eng.* 54(11):1940–1950, 2007. <https://doi.org/10.1109/TBME.2007.901024>.
  53. Dal Maso, F., P. Marion, and M. Begon. Optimal combinations of isometric normalization tests for the production of maximum voluntary activation of the shoulder muscles. *Arch. Phys. Med. Rehabil.* 97(9):1542–1551.e2, 2016. <https://doi.org/10.1016/j.apmr.2015.12.024>.
  54. Jensen, R. H., and D. T. Davy. An investigation of muscle lines of action about the hip: a centroid line approach vs the straight line approach. *J. Biomech.* 8(2):103–110, 1975. [https://doi.org/10.1016/0021-9290\(75\)90090-1](https://doi.org/10.1016/0021-9290(75)90090-1).
  55. Louis, N., and P. Gorce. Surface electromyography activity of upper limb muscle during wheelchair propulsion: influence of wheelchair configuration. *Clin. Biomech.* 25(9):879–885, 2010. <https://doi.org/10.1016/j.clinbiomech.2010.07.002>.
  56. Rincon, D. M., S. Ye, M. Rodriguez, and S. Nasser. Electromyographic activities of shoulder muscles during forward and reverse manual wheelchair propulsion. *Presented at the Thirs LACCEI International Latin American and Caribbean Conference for Engineering and Technology*, Catagena de Indias, Colombia, 2005, p. 7.
  57. Wakeling, J. M., et al. The energy of muscle contraction. I. Tissue force and deformation during fixed-end contractions. *Front. Physiol.* 11:813, 2020. <https://doi.org/10.3389/fphys.2020.00813>.
  58. Prado, L. G., I. Makarenko, C. Andresen, M. Krüger, C. A. Opitz, and W. A. Linke. Isoform diversity of giant proteins in relation to passive and active contractile properties of rabbit skeletal muscles. *J. Gen. Physiol.* 126(5):461–480, 2005. <https://doi.org/10.1085/jgp.200509364>.
  59. Ward, S. R., T. M. Winters, S. M. O'Connor, and R. L. Lieber. Non-linear scaling of passive mechanical properties in fibers, bundles, fascicles and whole rabbit muscles. *Front. Physiol.* 2020. <https://doi.org/10.3389/fphys.2020.00211>.
  60. Noonan, A. M., N. Mazara, D. P. Zwambag, E. Weersink, G. A. Power, and S. H. M. Brown. Age-related changes in human single muscle fibre passive elastic properties are sarcomere length dependent. *Exp. Gerontol.* 137:110968, 2020. <https://doi.org/10.1016/j.exger.2020.110968>.
  61. Lieber, R. L., E. Runesson, F. Einarsson, and J. Fridén. Inferior mechanical properties of spastic muscle bundles due to hypertrophic but compromised extracellular matrix material. *Muscle Nerve.* 28(4):464–471, 2003. <https://doi.org/10.1002/mus.10446>.
  62. Moo, E. K., T. R. Leonard, and W. Herzog. In vivo sarcomere lengths become more non-uniform upon activation in intact whole muscle. *Front. Physiol.* 2017. <https://doi.org/10.3389/fphys.2017.01015>.
  63. Sleboda, D. A., and T. J. Roberts. Internal fluid pressure influences muscle contractile force. *Proc. Natl. Acad. Sci.* 117(3):1772–1778, 2020. <https://doi.org/10.1073/pnas.1914433117>.
  64. Siebert, T., N. Stutzig, and C. Rode. A hill-type muscle model expansion accounting for effects of varying transverse muscle load. *J. Biomech.* 66:57–62, 2018. <https://doi.org/10.1016/j.jbiomech.2017.10.043>.
  65. Ryan, D. S., S. Domínguez, S. A. Ross, N. Nigam, and J. M. Wakeling. The energy of muscle contraction. II. Transverse compression and work. *Front. Physiol.* 2020. <https://doi.org/10.3389/fphys.2020.538522>.
  66. Moo, E. K., R. Fortuna, S. C. Sibole, Z. Abusara, and W. Herzog. In vivo sarcomere lengths and sarcomere elongations are not uniform across an intact muscle. *Front. Physiol.* 2016. <https://doi.org/10.3389/fphys.2016.00187>.
  67. Screen, H. R. C., D. L. Bader, D. A. Lee, and J. C. Shelton. Local strain measurement within tendon. *Strain.* 40(4):157–163, 2004. <https://doi.org/10.1111/j.1475-1305.2004.00164.x>.
  68. Thompson, M. S., M. N. Bajuri, H. Khayyeri, and H. Isaksson. Mechanobiological modelling of tendons: review and future opportunities. *Proc. Inst. Mech. Eng. H.* 231(5):369–377, 2017. <https://doi.org/10.1177/0954411917692010>.
  69. Wu, S. Y., W. Kim, and T. J. Kremen. In vitro cellular strain models of tendon biology and tenogenic differentiation. *Front. Bioeng. Biotechnol.* 2022. <https://doi.org/10.3389/fbioe.2022.826748>.
  70. Itoi, E., et al. Tensile properties of the supraspinatus tendon. *J. Orthop. Res.* 13(4):578–584, 1995. <https://doi.org/10.1002/jor.1100130413>.
  71. Matsushashi, T., et al. Tensile properties of a morphologically split supraspinatus tendon. *Clin. Anat.* 27(5):702–706, 2014. <https://doi.org/10.1002/ca.22322>.
  72. Fallon, J., F. T. Blevins, K. Vogel, and J. Trotter. Functional morphology of the supraspinatus tendon. *J. Orthop. Res.* 20(5):920–926, 2002. [https://doi.org/10.1016/S0736-0266\(02\)00032-2](https://doi.org/10.1016/S0736-0266(02)00032-2).
  73. Inoue, A., E. Chosa, K. Goto, and N. Tajima. Nonlinear stress analysis of the supraspinatus tendon using three-dimensional finite element analysis. *Knee Surg. Sports Traumatol. Arthrosc.* 21(5):1151–1157, 2013. <https://doi.org/10.1007/s00167-012-2008-4>.
  74. Åström, M. Laser Doppler flowmetry in the assessment of tendon blood flow. *Scand. J. Med. Sci. Sports.* 10(6):365–367, 2000. <https://doi.org/10.1034/j.1600-0838.2000.010006365.x>.
  75. Gobbi, A. *Bio-orthopaedics: A New Approach*. New York, NY: Springer Berlin Heidelberg, 2017.
  76. Hegedus, E. J., C. Cook, M. Brennan, D. Wyland, J. C. Garrison, and D. Driesner. Vascularity and tendon pathology in the rotator cuff: a review of literature and implications for rehabilitation and surgery. *Br. J. Sports Med.* 44(12):838–847, 2010. <https://doi.org/10.1136/bjism.2008.053769>.
  77. Docking, S., T. Samiric, E. Scase, C. Purdam, and J. Cook. Relationship between compressive loading and ECM changes in tendons. *Muscles Ligaments Tendons J.* 3(1):7–11, 2013. <https://doi.org/10.11138/mltj/2013.3.1.007>.
  78. Bossuyt, F. M., M. L. Boninger, A. Cools, N. Hogaboom, I. Eriks-Hoogland, and U. Arnet. Changes in supraspinatus and biceps tendon thickness: influence of fatiguing propulsion in wheelchair users with spinal cord injury. *Spinal Cord.* 2019. <https://doi.org/10.1038/s41393-019-0376-z>.
  79. Cook, J. L., and C. Purdam. Is compressive load a factor in the development of tendinopathy? *Br. J. Sports Med.* 46(3):163–168, 2012. <https://doi.org/10.1136/bjsports-2011-090414>.
  80. Parkinson, J., T. Samiric, M. Z. Ilic, J. Cook, J. A. Feller, and C. J. Handley. Change in proteoglycan metabolism is a characteristic of human patellar tendinopathy. *Arthritis Rheum.* 62(10):3028–3035, 2010. <https://doi.org/10.1002/art.27587>.
  81. Berenson, M. C., F. T. Blevins, A. H. K. Plaas, and K. G. Vogel. Proteoglycans of human rotator cuff tendons. *J. Orthop. Res.* 14(4):518–525, 1996. <https://doi.org/10.1002/jor.1100140404>.
  82. Vogel, K. G. What happens when tendons bend and twist? Proteoglycans. *J. Musculoskelet. Neuronal. Interact.* 4(2):202–203, 2004.
  83. Attia, M., et al. Alterations of overused supraspinatus tendon: a possible role of glycosaminoglycans and HARP/pleiotrophin in early tendon pathology. *J. Orthop. Res.* 30(1):61–71, 2012. <https://doi.org/10.1002/jor.21479>.

84. Fournier Belley, A., D. H. Gagnon, F. Routhier, and J.-S. Roy. Ultrasonographic measures of the acromiohumeral distance and supraspinatus tendon thickness in manual wheelchair users with spinal cord injury. *Arch. Phys. Med. Rehabil.* 98(3):517–524, 2017. <https://doi.org/10.1016/j.apmr.2016.06.018>.
85. Collinger, J. L., B. G. Impink, H. Ozawa, and M. L. Boninger. Effect of an intense wheelchair propulsion task on quantitative ultrasound of shoulder tendons. *PM&R.* 2(10):920–925, 2010. <https://doi.org/10.1016/j.pmrj.2010.06.007>.
86. Gil-Agudo, A., et al. Shoulder kinetics and ultrasonography changes after performing a high-intensity task in spinal cord injury subjects and healthy controls. *Spinal Cord.* 54(4):Art. no. 4, 2016. <https://doi.org/10.1038/sc.2015.140>.
87. Leclerc, M., C. Gauthier, R. Brosseau, F. Desmeules, and D. H. Gagnon. Changes to biceps and supraspinatus tendons in response to a progressive maximal treadmill-based propulsion aerobic fitness test in manual wheelchair users: a quantitative musculoskeletal ultrasound study. *Rehabil. Res. Pract.* 2021:e6663575, 2021. <https://doi.org/10.1155/2021/6663575>.
88. Bass, E. Tendinopathy: why the difference between tendinitis and tendinosis matters. *Int. J. Ther. Massage Bodyw.* 5(1):14–17, 2012.
89. Khan, K. M., J. L. Cook, J. E. Taunton, and F. Bonar. Overuse tendinosis, not tendinitis. *Physician Sportsmed.* 28(5):38–48, 2000. <https://doi.org/10.3810/psm.2000.05.890>.
90. Sonenblum, S. E., S. Sprigle, and R. A. Lopez. Manual wheelchair use: bouts of mobility in everyday life. *Rehabil. Res. Pract.* 2012:e753165, 2012. <https://doi.org/10.1155/2012/753165>.
91. Lalumiere, M., D. H. Gagnon, J. Hassan, G. Desroches, R. Zory, and D. Pradon. Ascending curbs of progressively higher height increases forward trunk flexion along with upper extremity mechanical and muscular demands in manual wheelchair users with a spinal cord injury. *J. Electromyogr. Kinesiol.* 23(6):1434–1445, 2013. <https://doi.org/10.1016/j.jelekin.2013.06.009>.
92. Qi, L., J. Wakeling, S. Grange, and M. Ferguson-Pell. Coordination patterns of shoulder muscles during level-ground and incline wheelchair propulsion. *J. Rehabil. Res. Dev.* 50(5):12, 2013. <https://doi.org/10.1682/jrrd.2012.06.0109>.
93. Lai, A. K. M., T. J. M. Dick, N. A. T. Brown, A. A. Biewener, and J. M. Wakeling. Lower-limb muscle function is influenced by changing mechanical demands in cycling. *J. Exp. Biol.* 224(3):jeb228221, 2021. <https://doi.org/10.1242/jeb.228221>.
94. Assila, N., S. Duprey, and M. Begon. Glenohumeral joint and muscles functions during a lifting task. *J. Biomech.* 126:110641, 2021. <https://doi.org/10.1016/j.jbiomech.2021.110641>.
95. Mazingo, J. D., et al. Shoulder mechanical impingement risk associated with manual wheelchair tasks in individuals with spinal cord injury. *Clin. Biomech.* 71:221–229, 2020. <https://doi.org/10.1016/j.clinbiomech.2019.10.017>.

**Publisher's Note** Springer Nature remains neutral with regard to jurisdictional claims in published maps and institutional affiliations.

Springer Nature or its licensor (e.g. a society or other partner) holds exclusive rights to this article under a publishing agreement with the author(s) or other rightsholder(s); author self-archiving of the accepted manuscript version of this article is solely governed by the terms of such publishing agreement and applicable law.